Enhanced numerical analysis of current-voltage characteristics of long wavelength infrared p-on-n HgCdTe photodiodes

K. JÓŹWIKOWSKI, M. KOPYTKO, and A. ROGALSKI*

Institute of Applied Physics, Military University of Technology, 2 Kaliskiego St., 00-908 Warszawa, Poland

Abstract. An enhanced original computer programme is applied to explain in detail the current-voltage characteristics of p-on-n long wavelength infrared (LWIR) HgCdTe photodiodes. The computer programme solves the system of non-linear continuity equations for carriers and Poisson equations. In the model ideal diode diffusion, generation-recombination, band-to-band tunnelling, trap-assisted tunnelling, and impact ionization are included as potential limiting mechanisms in the photodiodes. It is a clearly explained influence of extrinsic doping of an active device region on dark current-voltage characteristics and on R_0A product of HgCdTe photodiodes in a wide region of temperature and wavelengths. Special attention is directed to the dependence of tunnelling probability on the shape of potential barrier within the depletion region. The theoretical predictions are compared with experimental data of high quantity photodiodes published in the available literature.

Key words: enhanced numerical analysis, current-voltage characteristics, long wavelength infrared p-on-n HgCdTe photodiodes.

1. Introduction

Different HgCdTe photodiode architectures have been fabricated that are compatible with backside and frontside illuminated hybrid focal plane array (FPAs) technology. Generally, they can be divided into two families: n-on-p and p-on-n junctions.

The n-on-p junctions are fabricated in two different manners using Hg vacancy doping and extrinsic doping. Hg vacancies (V_{Hg}) provide intrinsic p-type doping in HgCdTe. In this case, the doping level depends on only one annealing temperature. However, the use of Hg vacancy as p-type doping is known to kill the electron lifetime, and the resulting detector exhibits a higher dark current than in the case of extrinsic doping use. However, for very low doping ($<10^{15}$ cm^{-3}), the hole lifetime becomes Shockley-Read limited and does not depend on doping anymore [1]. V_{Hg} technology leads to low minority diffusion length of the order of 10 to 15 μm, depending on the doping level. Generally, n-on-p vacancy doped diodes give rather high diffusion currents but leads to a robust technology as photodiode performance weakly depends on the doping level and absorbing layer thickness. Simple modelling manages to describe dark current behaviour of V_{Hg} doped n-on-p junctions over a range of at least eight orders of magnitude [2]. In the case of extrinsic doping, Cu, Au, and As are often used. Due to a higher minority carrier lifetime, extrinsic doping is used for low dark current (low flux) applications [3]. The extrinsic doping usually leads to a larger diffusion length and allows for a lower diffusion current but might exhibit performance fluctuations, thus affecting yield and uniformity.

In p-on-n photodiodes, also called double-layer heterojunction (DLHJ) structures, an absorber layer about 10 μm thick is n-type doped at 1×10^{15} cm^{-3} or less, and is sandwiched between the CdZnTe substrate and the highly arsenic-doped, wider-gap region. One important advantage of the p-on-n device is that the n-type Hg$_{1-x}$Cd$_x$Te carrier concentration is easy to control in the 10^{15} cm^{-3} range using extrinsic doping – usually indium or iodine (for the n-on-p device, the p-type carrier concentration at this low level is difficult). The wider band-gap capping Hg$_{1-y}$Cd$_y$Te ($y \approx x + 0.04$) is 0.5 to 1 μm thick. In the p-on-n photodiodes, the typical diffusion length is up to 30 μm to 50 μm for low doping levels and the dark currier generation is volume limited by the absorbing layer volume itself.

The different behaviour of saturation current depending on diffusion length is explained below. For an p-on-n diode structure, the junction resistance is limited by diffusion of minority carriers from the n side into the depletion region. In the case of conventional bulk diodes, where thickness of the active region $t \gg L_h$ (L_h is the minority diffusion length), the R_0A product is equal

$$(R_oA)_D = \frac{kT}{qJ_s} \frac{(kT)^{1/2}}{q^{3/2}n_i^2} N_D \left(\frac{\tau_p}{\mu_h}\right)^{1/2}, \qquad (1)$$

where J_s is the current density, n_i is the intrinsic carrier concentration, N_D is the doping concentration, and μ_h and τ_p are the minority carrier mobility and lifetime. The R_0A product (saturation current density) is proportional (inversely proportional) to $N_D\tau_p^{1/2}$. By thinning the active region to a thickness, d, smaller than the minority-carrier diffusion length (thus reducing the volume in which diffusion current is generated) the corresponding dark current decreases, provided that the back surface is properly passivated to reduce surface recombination. As a result, the current density can decrease

*e-mail: rogan@wat.edu.pl

K. Jóźwikowski, M. Kopytko, and A. Rogalski

by a factor of L_h/t. If the thickness of the n type region is such that $t \ll L_h$, we obtain:

$$(R_oA)_D = \frac{kT}{q^2}\frac{N_D}{n_i^2}\frac{\tau_p}{d}. \tag{2}$$

On the contrary, if $t \ll L_h$, the R_0A product (saturation dark current) is proportional (inversely proportional) to $N_D\tau_p$. Of course, analogical formulas can be obtained for n-on-p junctions.

In this paper an enhanced original computer programme is applied to explain in detail the current-voltage characteristics of p-on-n long wavelength infrared (LWIR) HgCdTe photodiodes. The computer programme solves the system of non-linear continuity equations for carriers and Poisson equations. The model includes ideal diode diffusion, generation-recombination, band-to-band tunnelling, trap-assisted tunnelling and impact ionization as potential limiting mechanisms in the HgCdTe photodiodes. The theoretical predictions are compared with experimental data of high quantity photodiodes published in the available literature.

2. Method of analysis

The analysis of photoelectric effects in semiconductor structures requires the solution of a set of transport equations that are comprised of the continuity equations for electrons and holes, Poisson's equation, and the thermal conductivity equation. The transport equations are given by [4, 5]:

$$\frac{\partial p}{\partial t} = -\frac{1}{q}\nabla\vec{j}_h + G - R, \tag{3}$$

$$\frac{\partial n}{\partial t} = \frac{1}{q}\nabla\vec{j}_e + G - R, \tag{4}$$

$$\nabla^2\Psi = -\frac{q}{\varepsilon\varepsilon_0}\left[N_D^+ - N_A^- + p - n\right] - \frac{1}{\varepsilon}\nabla\Psi\nabla\varepsilon, \tag{5}$$

$$C_V\frac{\partial T}{\partial t} - H = \nabla\chi \cdot \nabla T, \tag{6}$$

where Ψ is the electrostatic potential, j is the current density, q is the elementary charge, C_v is the specific heat, χ is the thermal conductivity coefficient, T is the temperature, G is the generation rate, R is the recombination rate, and H is the heat generation term. In the last term, a Joule heat is introduced as the heat generation. The indices n and p denote electron and hole, respectively.

In spite of the fact that the above equations are generally known, their solution represents serious mathematical and numerical problems. The reason for the difficulty is the non-linearity of these equations where carrier densities, ionized dopant densities as well as g-r factors are all complex functions of the electrostatic potential, Ψ and quasi-Fermi levels, $\Phi_{e,h}$. A number of articles have reported solution methods of this set of equations, starting from the work of Gummel [6] and de Mari [7], and ending with those adopted in commercial software packages [8, 9]. Independently, Jóźwikowski developed a set of numerical algorithms to solve the set of Eqs. (3)–(6). This method has been used for modelling many optoelectronic device structures [10–17].

The difference $G - R$ is the net generation of electron-hole pairs, and depends on all generation-recombination mechanisms. In this work $G - R$ is defined by

$$G - R = G_{THE} + G_{BTB} + G_{TAT} + G_{ION}, \tag{7}$$

where G_{THE} is the net thermal generation velocity, G_{BTB} is the net generation due to band-to-band tunnelling, G_{TAT} is the net generation due to trap-assisted tunnelling, and G_{ION} is the impact ionization generation. In this way we can introduce directly the tunnelling phenomena in transport equation to calculate both dark current as well as dynamic resistance of the photodiode. The first term in Eq. (7) includes Auger 1 and Auger 7, radiative and Shockley-Read-Hall (SRH) mechanisms. Including band-to-band tunnelling and impact ionization as the generation-recombination processes, G_{BTB} and G_{ION}, the thermal generation rate can be expressed as [15–17]:

$$G - R = \left[G_{ee}\frac{n}{n_0}\left(1 - \frac{np}{n_0p_0}\right) + G_{hh}\frac{p}{p_0}\left(1 - \frac{np}{n_0p_0}\right) + \right.$$
$$\left. + G_{RAD}\left(n_0p_0 - np\right) + (n_0 - n)\frac{1}{\tau_n^{SHR}}\right] + G_{BTB} + G_{ION} \tag{8}$$

G_{ee} and G_{hh} are thermal equilibrium generation rates due to electron-electron processes and hole-hole processes, respectively, and both can be expressed by lifetimes in intrinsic material defined by Auger 1 and Auger 7, respectively. G_{RAD} is the equilibrium radiative electron-hole pair generation rate. Detailed description of the above expressions can be found in Blakemore's monograph [18]. The last term in the quadratic bracket includes the influence of the SRH mechanism. The published lifetime for vacancy-doped HgCdTe material indicates that the SRH centre is donor-like, even though the metal vacancy is an acceptor. The expression for τ_n^{SHR} is derived in Appendixes A and B.

When the electric field in a semiconductor is increased above a certain value, the carriers gain enough energy (greater than the band gap) so that they can excite electron-hole pairs by impact ionization. In the local-field theory, the equation which governs the electron and hole impact ionization current is equal [19]

$$G_{ION} = \frac{1}{q}\alpha_e j_e + \frac{1}{q}\alpha_h j_h, \tag{9}$$

where α_e and α_h are functions only of the electric field at $\vec{r}$.

Experimentally, it has been found that the electron and hole ionization coefficients, in the limit of low field, can be represented by the expressions

$$\alpha(F) = a_e \exp\left(-b_e/F^{m_e}\right), \tag{10}$$

$$\beta(F) = a_h \exp\left(-b_h/E^{m_h}\right), \tag{11}$$

where m_e and m_h are close to unity at least at low field. The values of coefficients $a_e = 3 \times 10^5$ cm^{-1} and $a_h = 1.5 \times 10^5$ cm^{-1} are assumed after Kinch [20].

Current density is usually expressed as functions of quasi-Fermi levels:

$$\vec{j}_e = q\mu_e n\nabla\Phi_n, \tag{12}$$

$$\vec{j}_h = q\mu_h p\nabla\Phi_p, \tag{13}$$

where μ denotes the mobility and Φ is the quasi-Fermi level.

Enhanced numerical analysis of current-voltage characteristics of long wavelength infrared p-on-n HgCdTe photodiodes

In order to solve the set of transport Eqs. (3)–(7) with relations (8) and (9) using Newton's method, it is necessary to first linearise the equations and then employ an iteration algorithm that allows the calculation of small increments of Ψ, Φ_n, Φ_p, and T

$$\Psi = \Psi^0 + \delta\Psi,$$
$$\Phi_n = \Phi_n^0 + \delta\Phi_n,$$
$$\Phi_p = \Phi_p^0 + \delta\Phi_p,$$
$$T = T^0 + \delta T.$$

The remaining physical parameters in Eqs. (3)–(7) can be similarly expressed, for example:

$$n = n(\Psi, \Phi_n) = n^0 + \frac{\partial n}{\partial \Psi}\delta\Psi + \frac{\partial n}{\partial \Phi_n}\delta\Phi_n + \frac{\partial n}{\partial T}\delta T, \quad (14)$$

$$p = p(\Psi, \Phi_p) = p^0 + \frac{\partial p}{\partial \Psi}\delta\Psi + \frac{\partial p}{\partial \Phi_p}\delta\Phi_p + \frac{\partial p}{\partial T}\delta T, \quad (15)$$

$$G - R = G^0 - R^0 + \delta(G - R). \quad (16)$$

where

$$\delta(G-R) = \frac{\partial(G-R)}{\partial n}\left(\frac{\partial n}{\partial \Psi}\delta\Psi + \frac{\partial n}{\partial \Phi_n}\delta\Phi_n + \frac{\partial n}{\partial T}\delta T\right) +$$
$$+ \frac{\partial(G-R)}{\partial p}\left(\frac{\partial p}{\partial \Psi}\delta\Psi + \frac{\partial p}{\partial \Phi_p}\delta\Phi_p + \frac{\partial p}{\partial T}\delta T\right). \quad (17)$$

The set of Eqs. (3)–(7) can then be transformed into a set of algebraic equations and their solution allows the iterative calculation of corrections to electrical potential, quasi-Fermi levels, temperature, and consequently to other physical parameters.

3. Current-voltage characteristics: results and discussion

In this paper we consider high quality heterostructure p-on-n HgCdTe photodiode shown in Fig. 1. This photodiode structure is mainly addressed by liquid phase epitaxy (LPE), molecular beam epitaxy (MBE) or metalorganic chemical vapour deposition (MOCVD) on a lattice-matched CdZnTe substrate.
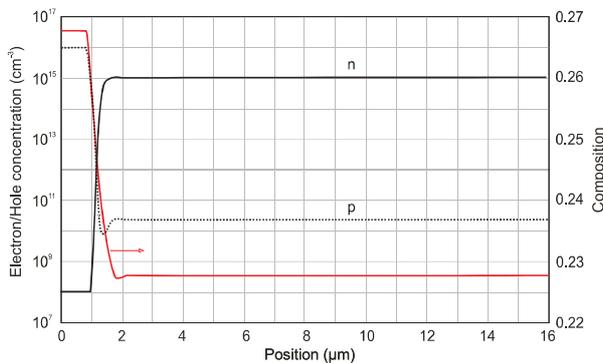

Fig. 1. Equilibrium carrier concentration and composition profiles across an p-on-n HgCdTe photodiode structure in the absence of bias voltage

The doping profiles of p-on-n HgCdTe photodiode are shown in Fig. 1. One important advantage of the p-on-n de-

vice in comparison with n-on-p structure is that the n-type $Hg_{1-x}Cd_x Te$ carrier concentration is easy to control in the 10^{15} cm^{-3} range using extrinsic doping – usually indium or iodine (for the n-on-p device, the p-type carrier concentration at this low level is difficult to achieve). The wider band-gap p-type capping $Hg_{1-y}Cd_y Te$ (y $\approx$ x + 0.04) is 0.5 to 1 μm thick not intentionally doped. The structures are terminated with a thin (500 Å) CdTe layer for protection of the surface. n-type HgCdTe epitaxial layer with carrier concentration about 10^{15} cm^{-3} is about 15-μm thick and is grown on a CdZnTe substrate. The photodiode is backside illuminated and exhibits high quantum efficiency because the thickness of the base layer is thin compared to the minority carrier diffusion length.

In ideal photodiodes the diffusion current is dominant, therefore their saturation current is very low and insensitive to the detector bias. Usually however, many additional excess mechanisms affect the dark current of HgCdTe photodiodes [21]. They arise from non-fundamental sources located in the base and cap layer, the depletion region and the surface. As the operating temperature is lowered, the thermal dark current mechanisms become weaker and allow other mechanisms to prevail. The main leakage mechanisms of HgCdTe photodiodes are generation in the depletion region, interband tunnelling, trap-assisted tunnelling, and impact ionization. Some of them are caused by structural defects in the p-n junction. These mechanisms now receive much attention, particularly because they determine ultimately the array uniformity, yield and cost for some applications, especially those with lower operating temperatures. However, clear evidence of pure generation in the depletion region has never been observed in high quality HgCdTe photodiodes.
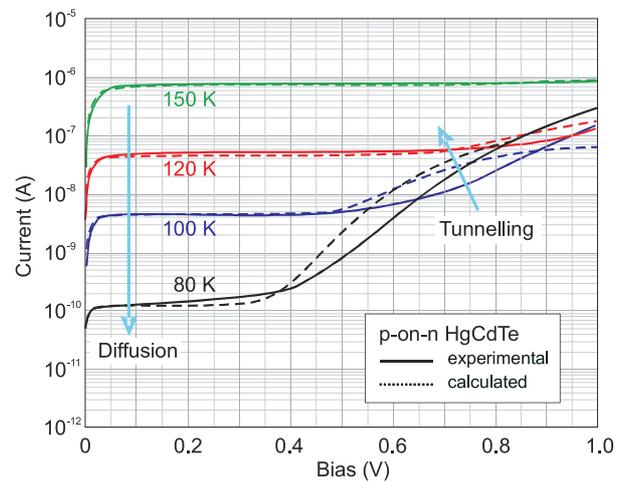
Fig. 2. The reverse biased $I--V$ characteristics of p-on-n HgCdTe photodiode at 80 K, 100 K, 120 K and 150 K ($\lambda_c = 9.7$ μm at 77 K, 30 μm pitch). The experimental data after Ref. 2 are compared with theoretical predictions

As an example, Fig. 2 compares the experimental LETI's data with theoretical predictions for long wavelength IR (LWIR) p-on-n HgCdTe photodiode ($\lambda_c = 9.7$ μm at 77 K, 30 μm pitch, 0° FOV), where diffusion, impact ionization, and

tunnelling (band-to-band and trap-assisted tunnelling) mechanisms are taken into account. The material parameters taken in calculations are given in Table 1. As is shown in Fig. 2, thermal current strongly decreases with temperature in the range of low biases. At the higher biases, the current exhibits the opposite thermal behaviour. This behaviour is explained by contribution of tunnelling current since the tunnelling probability depends on energy gap and increases with HgCdTe temperature decreasing. In order to minimize tunnelling current, a low doping level is preferable on at least one side of the junction. The better agreement with experimental data has been achieved for a triangular barrier. Due to low doping level of n-type base region ($N_D = 10^{15}$ cm^{-3}), it does not lead to a significant tunnelling current which illustrates the role of an p-type cap layer.

Table 1

Material parameters for p-on-n HgCdTe photodiode at 77 K assumed in calculations

Cutoff wavelength (μm)	9.7
Absorber x value	0.228
Cap x value	0.268
Absorber thickness (μm)	15
Cap thickness (μm)	1
Electron concentration in absorber (cm^{-3})	1×10^{15}
Hole concentration in cap layer (cm^{-3})	1×10^{16}
Dislocations density in bulk (cm^{-2})	10^5
Hg vacancies in cap layer (cm^{-3})	10^{15}

An additional insight in the saturation dark current of p-on-n HgCdTe photodiodes gives Fig. 3, where the influence of carrier concentrations in active and cap regions on reverse dark current is shown for 9.7-μm photodiode operated at 80 K. From this figure results, that the best agreement between experimental data and theoretical predictions has been achieved assuming doping concentrations in cap and active region equal 10^{16} cm^{-3} and 10^{15} cm^{-3}, respectively.
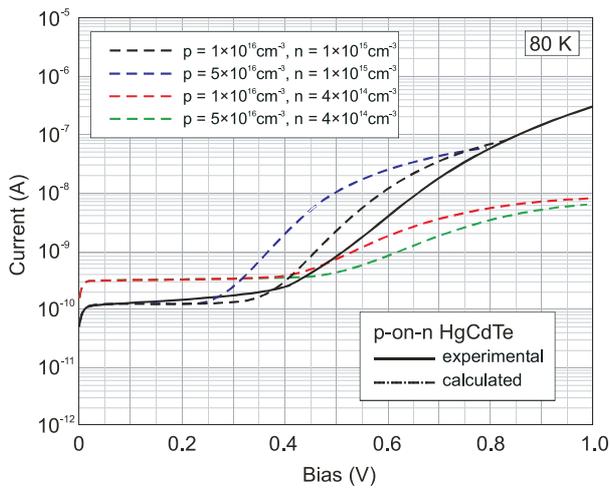

Fig. 3. The reverse biased $I--V$ characteristics of p-on-n HgCdTe photodiode at 80 K for different carrier concentration ($\lambda_c = 9.7$ μm at 77 K, 30 μm pitch)

4. Tunnelling as the generation-recombination process

Interband tunnelling processes contribute to the leakage currents and noise in reverse-biased infrared photodiodes' [21]. Therefore, numerical analysis of these effects in semiconductor devices becomes essential. The existing methods represent one-dimensional models and are typically based on the WKB approximation and Kane's model [22, 23]. Accurate calculations of tunnelling currents for a general diode structure require triple integration for each bias [24], which is too complex for practical modelling algorithms. Adar proposed a method for the calculation of tunnelling currents [25]. His approach, called spatial tunnelling integration (STI), contains only one integration step through the depletion layer for a given bias and can be used for any semiconductor structure. This algorithm relies on the specific shape of Kane's barrier across the energy gap, and thus is highly accurate when applied to narrow-gap semiconductors. Integration of band-to-band tunnelling currents originating from two-dimensional (2D) or three-dimensional (3D) electric-field structures is theoretically difficult, since the tunnelling transition probability used in the WKB approximation is essentially one dimensional (1D). An important feature of Adar's STI technique is the possibility to extend its use to 2D or 3D problems in a natural way (see Fig. 4). By using the STI procedure Adar has obtained the following simplified tunnelling current calculation formalism:

$$j_T = \int\limits_{\vec{r}_L}^{\vec{r}_R} q G_T \left[F\left(\vec{r}\right) \right] \Delta f_{FD}\left(\vec{r}\right) d\vec{r}, \qquad (18)$$

where F is the electric field in the depletion region, G_T represents the tunnelling generation function, and $\Delta f_{FD}\left(\vec{r}\right)$ is the filling probability of states in conduction and valence bands. Its shape is given in Appendix C of Ref. 16.
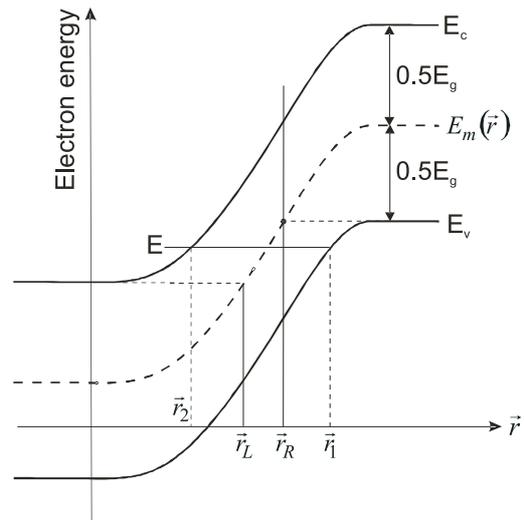

Fig. 4. Band structure of a p-n junction. E_m is the midgap energy. $\vec{r}_L$ and $\vec{r}_R$ define the region (shaded) where the midgap energy $E_m(\vec{r})$ is allowed for reverse-direct tunnelling. In the traditional method, for a given electron energy E, calculation of two reverse points, $\vec{r}_1$ and $\vec{r}_2$, creates serious numerical difficulties

In the case of a one-dimensional case (y-direction), the tunnelling generation is given by

$$G_{Ty}(F) = \frac{\sqrt{2}q^2\sqrt{m^*}F_y^2}{4\pi^3\hbar^2\sqrt{E_g}}\exp\left(-\frac{\pi\sqrt{m^*}E_g^{3/2}}{2\sqrt{2}q\hbar F_y}\right). \quad [A/m^3]$$

(19)

where F_y represents the electric-field component in the y direction.

The algorithm scans the numerical grid to find points of local extremes of electric-field components (for example, in the $y$direction). Next, it checks if direct band-to-band tunnelling from valence band to conduction band (or opposite) is possible. If the probability is nonzero, then the $y$component of the tunnelling current can be obtained from Eq. (18). Since the band-to-band tunnelling process can be regarded as generation recombination of electron-hole pairs, taking place between points r_L and r_R, then expression (18) describes precisely the tunnelling generation velocity at a specific point contributing to the $y$component of the tunnelling current. In the same manner components of tunnelling currents in the x and z directions can be obtained. The resulting tunnelling generation velocity can be expressed by

$$G_T = \left(G_{Tx}^2 + G_{Ty}^2 + G_{Tz}^2\right)^{1/2}. \quad (20)$$

Using this approach, the tunnelling process can be represented as a generation-recombination process taking place in the areas of built-in electric fields and consequently added to the g-r component in the continuity equations. It is evident that the tunnelling factor is a function of the electrical potential and its gradient, as well as the quasi-Fermi levels for electrons and holes and the sample temperature. The tunnelling process affects the spatial distribution of all these parameters and its implementation in the transport equations allows for the calculation of the device characteristics.

The tunnelling probability depends strongly on the shape of a potential barrier. The usual direct tunnelling calculations assume a particle of constant effective mass incident on a triangular or parabolic potential barrier. The expression (19) has been obtained for the parabolic barrier. In the Kane's paper it has a form as below [22]

$$G_T(F) = \frac{q^2\sqrt{m^*}F^2}{18\pi\hbar^2\sqrt{E_g}}\exp\left\{-\frac{\pi\sqrt{m^*}E_g^{3/2}}{2q\hbar F}\right\}. \quad [A/m^3]$$

(21)

and is virtually similar to Eq. (19) except for the numerical constant.

Using a procedure described by Moll [26] and STI technique, the tunnelling generation for triangular barrier can be obtained as (see Appendix C)

$$G_{Ty}(F) = \frac{q^2\sqrt{m^*}F_y^2}{4\sqrt{2}\pi^2\hbar^2\sqrt{E_g}}\exp\left(-\frac{4\sqrt{2m^*}E_g^{3/2}}{3q\hbar F_y}\right). \quad [A/m^3]$$

(22)

Figure 5 shows the thermal and tunnelling rate profiles of reverse biased ($U = -0.6$ V) LWIR p-on-n HgCdTe photodiode at 80 K ($\lambda_c = 9.7$ μm at 77 K, 30 μm pitch, $0°$ FOV). In spite of the higher doping level of the front p-type cap layer

($p = 10^{16}$ cm^{-3}), the influence of Auger 1 mechanism on thermal generation is considerably suppressed due to higher band gap energy of this region. In the p-type base layer of the photodiode with acceptor concentration of 10^{16} cm^{-3} the Auger 7 mechanism is decisive. Of course, in the depletion region the tunnelling generation and impact ionization achieve their maximum.
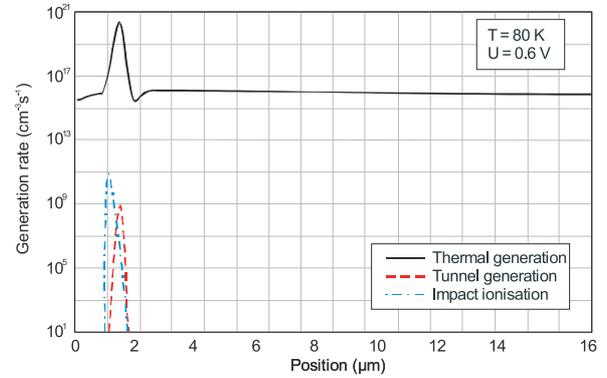

Fig. 5. Distribution of thermal and tunnelling generation rates vs. position for reverse biased ($U = 0.6$ V) p-on-n HgCdTe photodiode at 80 K ($\lambda_c = 9.7$ μm at 77 K, 30 μm pitch, $0°$ FOV)

5. R_0A product

The minority carrier lifetime in purely V_{Hg}-doped p-type HgCdTe material is limited by the SRH mechanism. The lifetime data for this material indicates that the SRH centre is donor-like, even though the Hg vacancy is an acceptor. In order to estimate the level of SRH generation, the density of trap centres and their ionization energies must be known, both of which are difficult to measure and are usually estimated from carrier lifetime measurements. In the calculations used in this paper, it has been assumed that the trap density is uniform across the device and changes between 10^{12} and 10^{14} cm^{-3}, with ionization energy equal to $0.7Eg$ as measured from the top of the valence band. The assumed SRH recombination model for Hg vacancy-doped material is described in Appendix A.

Extrinsically doped p-type HgCdTe material containing no vacancies exhibits considerably longer minority carrier lifetimes than purely V_{Hg}-doped material. The SRH centre appears to be acceptor-like or neutral, located approximately at the intrinsic level. Typically in LWIR material for the doping concentration $p < 10^{16}$ cm^{-3}, the measured lifetime is dominated by the SRH mechanism, but for $p > 10^{16}$ cm^{-3} Auger dominates [20, 21].

However, in the case of p-on-n HgCdTe photodiodes, the contribution of thermal generation in the wider bandgap p-type cap layer is suppressed. Figure 5 indicates that the cap layer contributes a negligible amount of thermally generated diffusion current compared with that from an n-type absorber layer at 77 K. As a result, the decisive influence on the value of R_0A product of p-on-n junctions has n-type active region, where Auger 1 mechanism is dominant.

Figure 6 presents the dependence of R_0A product on cutoff wavelength at 78 K for photodiode doping profile shown in

Fig. 1 (composition of active region is changed in dependence on cut-off wavelength). Influence of radiative recombination mechanism is negligible in comparison with contribution of Auger 1 process. The overlap matrix elements $|F_1F_2|$ cause the biggest uncertainly in the Auger lifetime. Recently published paper by Grein *et al.* [27] concerning the modelling of Auger mechanisms in HgCdTe ternary alloy indicates that the resulting values are well fitted to the extensively employed Beattie, Landsberg, and Blakemore (BLB) expression with the values of the overlap matrix elements $|F_1F_2|$ near the lower end of the range of values (0.1 to 0.3) that have been historically used. The reasonable agreement with BLB's Auger1 formula, has been obtained by adjusting the overlap integral of the Bloch functions $|F_1F_2|$ to 0.16. It is shown that the predicted lifetimes, and hence $|F_1F_2|$ values, depend significantly on effective masses and thus the accuracy of the theoretical predictions is dependent on the accuracy of the experimentally determined electronic structure properties. The curves in Fig. 6 are calculated assuming $|F_1F_2|$ values equal 0.2 as well as 0.16. Also influence of ohmic and non-ohmic photodiode contacts are presented assuming contact recombination rates equal 10^4 and 10^2 cm/s, respectively. Difference between particular R_0A-curves are emphasized with cut-off wavelength decreasing.
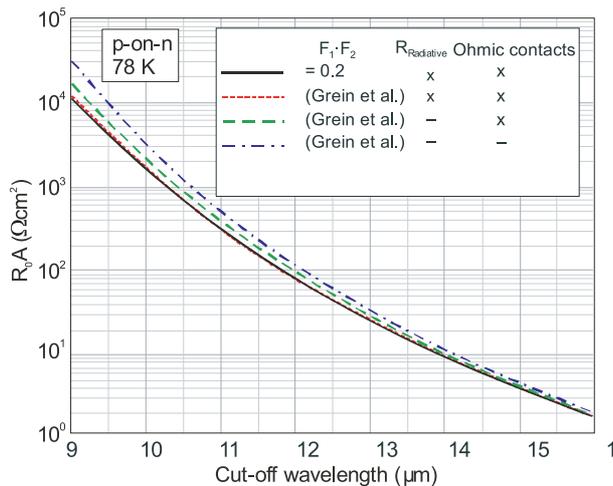

Fig. 6. Dependence of the R_0A product on cut-off wavelength for p-on-n LWIR HgCdTe photodiodes at 78 K assuming different combination of parameters

Interesting results are gathered in Fig. 7, where the experimental data and theoretically preceded lines are calculated for p-on-n HgCdTe photodiodes. Difference between our theoretical prediction and the Teledyne empirical model [32] is small. Upper experimental data coincide very well with theoretical predictions. In general however, considerably scattering in experimental R_0A data is observed. Raytheon [28] and BAE [30] data is obtained on mesa heterostructures on As/In-doped LPE grown material. Teledyne data (formerly Rockwell) [29] is based on planar diodes fabricated by As-

implantation in In-doped MBE-grown layers. Instead Selex data [31] is for As and In MOCVD doped p-on-n junctions. Finally, several points obtained at LETI are for As ion implanted diodes on In-doped LPE-grown layers.
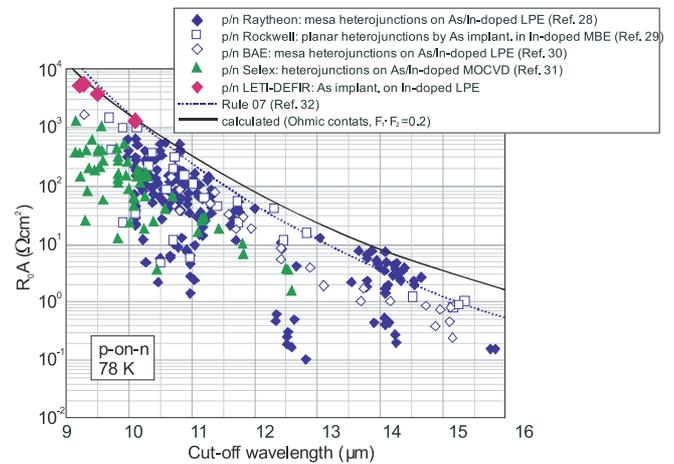
Fig. 7. R_0A product of p-on-n LWIR HgCdTe photodiodes at 77 K. The experimental values are according to Ref. 2 (LETI-DEFIR). Doted line – Teledyne empirical model (after Ref. 32); solid line – our model assuming an ohmic contacts, radiative and Auger ($F_1F_2 = 0.2$) processes

6. Conclusions

In this paper an enhanced original computer programme is applied to explain in detail the current-voltage characteristics of p-on-n LWIR HgCdTe photodiodes. The computer programme solves the system of non-linear continuity equations for carriers and Poisson equations. In the model ideal diode diffusion, generation-recombination, band-to-band tunnelling, trap-assisted tunnelling, and impact ionization are included as potential limiting mechanisms in the HgCdTe photodiodes. The model clearly explains the influence of doping of an active device region on R_0A product of HgCdTe photodiodes in a wide range of wavelengths.

In comparison with p-on-n photodiodes, the vacancy doped photodiodes (n-on-p structure) exhibit higher dark currents [2]. Despite this fact, n-on-p technology is a viable solution for operation in a high flux configuration where the dark current is not an issue. This technology assures small fluctuations (scattering) of the measured R_0A products. p-on-n photodiode design leads to lower dark currents. Such low dark current photodiodes, being closer to intrinsic material limits, may also be affected by lower energy perturbation enhancing also the scatter in R_0A data.

In the paper, an attention is directed to the dependence of tunnelling probability on the shape of a potential barrier in the depletion region. It is shown that the tunnelling current is decisive for reverse bias voltages above 0.3 V. A better agreement of theoretically predicted curves with experimental data has been achieved for a triangular barrier.

Appendix A

SRH recombination model for Hg-vacancy doped HgCdTe

The minority carrier lifetime in vacancy-doped material is limited by an SRH mechanism. In our model we assume that the Hg-vacancy is equivalent to an atom with a charge of $-2q$, and the unfilled bond can be treated as two holes each with charge $+q$. These unfilled bonds create two levels of energy. One of them is located near the top of the valence band and is an acceptor level, instead the second is deep trap level with an ionization energy equal to $0.7E_g$ (above a half of energy gap) (see Fig. A1).
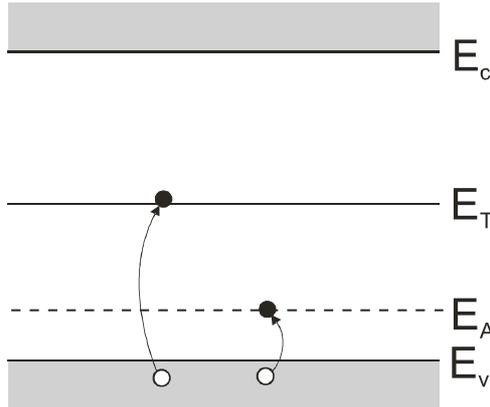

Fig. A1. Double ionisation of Hg-vacancy. The acceptor level, E_A, and trap level, E_T, are occupied by electrons

The grand thermodynamic potential in unit volume for mercury vacancies with a snatched electron at the energy level E_A should assume the minimum value at the equilibrium condition and can be expressed as

$$\Omega_A = (-X - q\Psi - E_g + E_A)\,N_T f_A - k_B T \ln W_A - \\ -\Phi_i N_T f_A = \min,$$
(A1)

where X is the electron affinity, Ψ is the electrical potential, N_T is the concentration of Hg vacancies, f_A is the distribution function, and W_A is the number of state ways in which $N_T f_A$ acceptor levels are ionized. W_A is equal to

$$W_A = \beta^{N_T f_A} \frac{N_T!}{(N_T f_A)!\,[N_T (1 - f_A)]!},$$
(A2)

where β is the number of distribution ways of valence electrons in binding orbitals coupled with Hg vacancy. If we assume that absent of Hg atom prompts absence of two electrons, then four states in $p_x -$ and p_y-orbitals can be occupied in six ways. For this reason we assume that $\beta = 6$.

Using Stirling's equation for Eq. (A2) and Euler-Lagrange's condition for Eq. (A1), the following expression for equilibrium distribution function can be obtained

$$f_A^0 = \frac{1}{1 + (1/\beta)\exp\left[(-X - e\Psi - E_g - \Phi_i)/k_B T\right]},$$
(A3)

which determines equilibrium distribution function and defines electron probability to occupy accepted levels, E_A, of Hg vacancy. Φ_i is the Fermi level.

In the nonequilibrium condition, the distribution function is equal to

$$f_A = \frac{1}{1 + (1/\beta)\exp\left[(-X - q\Psi - E_g + E_A - \Phi_n)/k_B T\right]},$$
(A4)

where Φ_n is the electron Fermi quasi-level. Due to low ionization energy, E_A, the Hg-vacancy acceptor levels are occupied by electrons.

The grand thermodynamic potential in the unit volume for mercury vacancies with a snatched electron at the trap energy E_T should assume the minimum value at the equilibrium condition and can be expressed as

$$\Omega_T = (-X - q\Psi - E_g + E_T - \Phi_i)\,N_T f_T - k_B T \ln W_T = \min.$$
(A5)

Analogical considerations as for Ω_A provide the following expression

$$f_T^0 = \frac{1}{1 + (1/\alpha)\exp\left[(-X - q\Psi - E_g + E_T - \Phi_i)/k_B T\right]}.$$
(A6)

It is the equilibrium distribution function which determines an electron's occupation probability on the trap energy level of Hg vacancy, E_T. Because in practice all acceptor levels of Hg vacancies are occupied by electrons, then in p_x- i p_y-bonding orbitals four states can be occupied by three electrons in four ways. Therefore we assume that $\alpha = 4$.

In a similar way as previously, for the nonequilibrium conditions

$$f_T = \frac{1}{1 + (1/\alpha)\exp\left[(-X - q\Psi - E_g + E_T - \Phi_n)/k_B T\right]}.$$
(A7)

Following the treatment given by Shockley and Read [33], the net rate of electron trapping can be expressed as:

$$R_n = c_n N_T \left[n\,(1 - f_T) - \frac{1}{\alpha} n_1 f_T \right],$$
(A8)

where

$$n_1 = n_0 \exp\left(\frac{-X - q\Psi - E_g + E_T - \Phi_i}{k_B T} \right).$$
(A9)

Similarly, the net rate of hole trapping is equal to

$$R_p = c_p N_T \left[p f_T - p_1 \alpha\,(1 - f_T) \right],$$
(A10)

where

$$p_1 = p_0 \exp\left(\frac{X + q\Psi + E_g - E_T + \Phi_i}{k_B T} \right).$$
(A11)

c_n and c_p are the electron and hole capture rates, respectively; and n_0 and p_0 are the equilibrium electron and hole concentrations, respectively.

Under steady state conditions, the rate of electron-hole pair recombination R is constant and equal to $R = R_n = R_p$. From Eqs. (A8) and (A10), the last condition results in

$$R = \frac{np - n_0 p_0}{\tau_{p_0}\left(n + \alpha^{-1} n_1\right) + \tau_{n_0}\left(p + \alpha p_1\right)},$$
(A12)

where

$$c_n = \frac{1}{\tau_{n_0} N_T}, \qquad (A13)$$

$$c_p = \frac{1}{\tau_{p_0} N_T}. \qquad (A14)$$

The term τ_{n0} is the lifetime for electrons injected into highly p-type specimens and τ_{p0} is the lifetime for holes injected into highly n-type specimens. In the calculations, the values of $c_n = 1.5 \times 10^{-7}$ cm^{3}s^{-1} and $c_p = 3 \times 10^{-9}$ cm^{3}s^{-1} are used after Nemirovsky *et al.* [34].

Between the excess carrier concentrations the following approximate condition is fulfilled

$$\Delta n + N_T \Delta f_T = \Delta p, \qquad (A15)$$

where Δf_T is the change of occupation probability of a trap level. Because $\Delta n \neq \Delta p$, then the electron and hole lifetimes are different, and

$$R = \frac{\Delta n}{\tau_n^{SHR}} = \frac{\Delta p}{\tau_p^{SHR}}. \qquad (A16)$$

In steady state conditions, $R_n = R_p$, and

$$\Delta f_T = \frac{c_n \left(1 - f_T^0\right) - c_p f_T^0}{c_p f_T^0 N_T + c_p \left(p_0 + \alpha_{p_1}\right) + c_n \left(n_0 + \alpha^{-1} n_1\right)} \Delta n, \qquad (A17)$$

$$\Delta f_T = \frac{c_n \left(1 - f_T^0\right) - c_p f_T^0}{c_n \left(1 - f_T^0\right) N_T + c_p \left(p_0 + \alpha_{p_1}\right) + c_n \left(n_0 + \alpha^{-1} n_1\right)} \Delta p, \qquad (A18)$$

and taking further into account

$$f_T = f_T^0 + \Delta f_T, \quad n = n_0 + \Delta n, \quad p = p_0 + \Delta p, \qquad (A19)$$

we obtain

$$np - n_0 p_0 = n_0 \Delta p + p_0 \Delta n = (n_0 + p_0) \Delta n + $$
$$+ n_0 N_T \Delta f_T = (n_0 + p_0) \Delta p - p_0 N_T \Delta f_T. \qquad (A20)$$

Finally, we can achieve the SRH expressions for carrier lifetimes, for electrons and holes:

$$\tau_n^{SHR} = $$
$$= \frac{\tau_{n0} f_T^0 N_T + \tau_{n0} \left(p_0 + \alpha p_1\right) + \tau_{p0} \left(n_0 + \alpha^{-1} n_1\right)}{f_T^0 \left(1 - f_T^0\right) N_T + \left(1 - f_T^0\right) \left(p_0 + \alpha p_1\right) + f_T^0 \left(n_0 + \alpha^{-1} n_1\right)}, \qquad (A21)$$

$$\tau_p^{SHR} = $$
$$= \frac{\tau_{p0} \left(1 - f_T^0\right) N_T + \tau_{n0} \left(p_0 + \alpha p_1\right) + \tau_{p0} \left(n_0 + \alpha^{-1} n_1\right)}{f_T^0 \left(1 - f_T^0\right) N_T + \left(1 - f_T^0\right) \left(p_0 + \alpha p_1\right) + f_T^0 \left(n_0 + \alpha^{-1} n_1\right)}. \qquad (A22)$$

If additional recombination mechanisms take place, the effective carrier lifetimes for electrons and holes are given by

$$\tau_n = \frac{1}{\left(G_{ee} \dfrac{n}{n_0^2 p_0} + G_{hh} \dfrac{p_0}{n_0 p_0^2} + G_{RAD} \dfrac{1}{n_0 p_0}\right) \gamma + \dfrac{1}{\tau_n^{SHR}}}, \qquad (A23)$$

$$\tau_p = \frac{1}{\left(G_{ee} \dfrac{n}{n_0^2 p_0} + G_{hh} \dfrac{p_0}{n_0 p_0^2} + G_{RAD} \dfrac{1}{n_0 p_0}\right) \delta + \dfrac{1}{\tau_p^{SHR}}}, \qquad (A24)$$

where

$$\gamma = n_0 + p_0 + $$
$$+ n_0 N_T \frac{\tau_{p0} \left(1 - f_T^0\right) - \tau_{n0} f_T^0}{\tau_{n0} f_T^0 N_T + \tau_{n0} \left(p_0 + \alpha p_1\right) + \tau_{p0} \left(n_0 + \alpha^{-1} n_1\right)}, \qquad (A25)$$

and

$$\delta = n_0 + p_0 + p_0 N_T \cdot $$
$$\cdot \frac{\tau_{n0} f_T^0 - \tau_{p0} \left(1 - f_T^0\right)}{\tau_{p0} \left(1 - f_T^0\right) N_T + \tau_{n0} \left(p_0 + \alpha p_1\right) + \tau_{p0} \left(n_0 + \alpha^{-1} n_1\right)}. \qquad (A26)$$

In the above equations, G_{ee} is the coefficient of the Auger 1 recombination, G_{hh} is the coefficient of the Auger 7 process, and G_{RAD} is the coefficient of radiative process. The definition of these coefficients is given in Blakemore's monograph [18]. The expression of G_{RAD} is taken from Ref. 35. HgCdTe material parameters necessary in calculations are given in Ref. 21.

Appendix B

The influence of an electric field on the kinetic of SRH processes

Figure B1 shows three kinds of electric-field-assisted emissions from a Coulomb's well. Arrows indicate the possible mechanisms of electron and hoe emissions: Frenkel-Poole emission, pure tunnelling from trap level into conduction or valence bands, and phonon assisted tunnelling.

The electron emission from the level E_T to the conduction band is possible if energy $E_g - E_T$ is delivered for the electron. The filling of level E_T by an electron with valence band is equivalent transition of the hole with the level E_T to the valence band and require the overcoming of the energy barrier equal to E_T. The external electric field causes an inclination of energy bands and stimulates a changing of distribution of the potential energy around the mercury vacancy. In consequence, the electric field enhances a generation-recombination process around the mercury vacancy through the decreasing of energy required both for the emission of an electron with energy level E_T to the conduction band as well as for emission of a hole with the empty level E_T to the valence band. Because the trapping rate is strongly dependent on ionization energy, the electric field can essentially influence τ_{n0} and τ_{p0} values, which are inversely proportional to trapping rates. The capture coefficients, c_n and c_p, are connected with emission coefficients, e_n^0 and e_p^0, and for electrons

$$e_n^0 = c_n \alpha^{-1} n_0 \exp\left[\left(-X - q\Psi - E_g + E_T - \Phi_i\right)/k_B T\right]. \qquad (B1)$$

Enhanced numerical analysis of current-voltage characteristics of long wavelength infrared p-on-n HgCdTe photodiodes
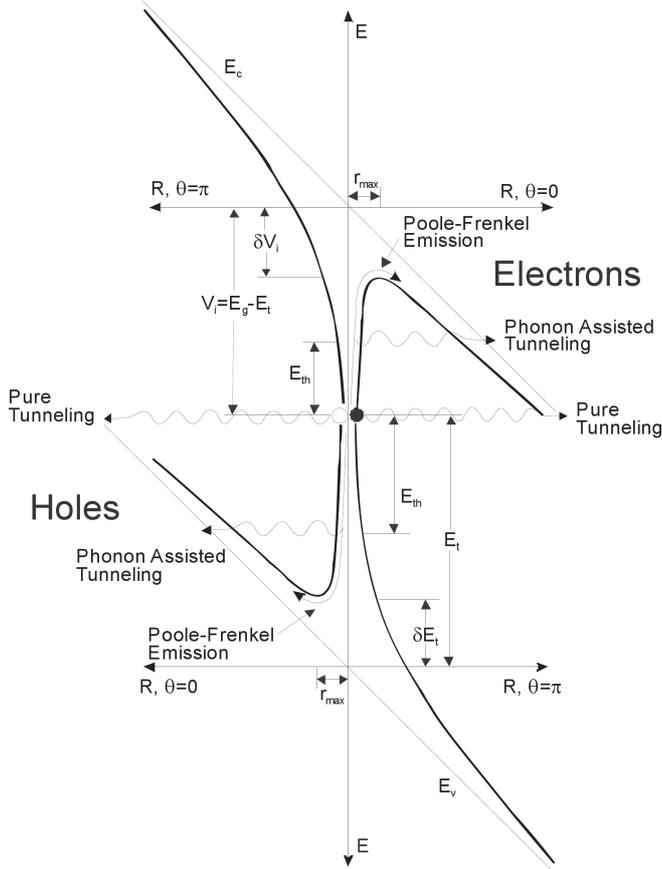

Fig. B1. Three mechanisms increasing the emission rate from trap levels in mercury vacancy caused by an external (or built-in) electric field: Poole-Frenkel emission, pure tunnelling from trap level into conduction or valence bands, and phonon-assisted tunnelling. Taking into account these mechanisms the c_n and c_p parameters are modified

Using the Boltzmann statistic

$$n_0 = N_c \exp\left[(X + q\Psi + \Phi_i)/k_B T\right], \qquad (B2)$$

where N_c is the effective density of the conduction band states.

From the last two equations result in

$$e_n^c = c_n \alpha N_c \exp\left[-(E_g - E_T)/k_B T\right]. \qquad (B3)$$

But $E_g - E_T = E_i$ is the ionization energy of electron emission with level E_T to the conduction band. If the electric field decreases E_i barrier by ΔE_i, then the emission coefficient increases according to

$$e_n = e_n^0 \exp\left(\Delta E_T/kT\right). \qquad (B4)$$

Obviously, the capture coefficient also increases by a similar factor

$$c_n = c_n^0 \exp\left(\Delta E_T/kT\right). \qquad (B5)$$

This phenomenon is named the Poole-Frenkel effect.

The electron electrostatic energy in the trap region localized in point $r = 0$ in uniform external electric field F directed along the z-axis can be expressed as

$$V(r) = -\frac{q^2}{4\pi\varepsilon_r\varepsilon_0 r} - qFr\cos\Theta. \qquad (B6)$$

Decreasing of energy barrier in this case is equal to

$$\Delta E_i(\Theta) = \frac{q^{3/2} F^{1/2} (\cos\Theta)^{1/2}}{(\pi\varepsilon_r\varepsilon_0)^{1/2}}. \qquad (B7)$$

In the case of the three-dimensional (3D) Hartke's model [36], the increasing factor of electron emission rate with the trap level is equal

$$\frac{(e_n)_{P-F}}{e_n^0} = \frac{1}{4\pi}\int_0^{2\pi} d\phi \int_0^{\pi} \sin\Theta d\Theta \exp\left[-\Delta E_i(\Theta)/kT\right]. \qquad (B8)$$

Analogical considerations for the hole emission coefficient provide the following equation

$$e_p^0 = c_p \alpha^{-1} p_0 \exp\left[(-X + q\Psi + E_g - E_T + \Phi_i)/k_B T\right]. \qquad (B9)$$

The hole potential energy in the trap region is equal to

$$V(r) = -\frac{q^2}{4\pi\varepsilon_r\varepsilon_0 r} + qFr\cos\Theta. \qquad (B10)$$

The hole emission is the equivalent excitation of the electron with the valence band into the trap level. It can be easily noticed, the Poole-Frenkel effect for holes provides to identical reduction of barrier as for electron emission, and therefore

$$\frac{(e_p)_{P-F}}{e_p^0} = \frac{(e_n)_{P-F}}{e_n^0}. \qquad (B11)$$

Rosencher *et al.* [37] have obtained 3D expression for electron emission rate in the trap assisted tunnelling process. This expression can be used to determine electron emission rates from trap level, $(e_n)_{TAT}$ and $(e_p)_{TAT}$, for electrons and holes:

$$(e_n)_{TAT}, (e_p)_{TAT} = \frac{1}{2\pi}\int_0^{2\pi} d\phi \int_0^{\pi/2} \left(\frac{U}{3\hbar}\right)\left(\frac{U}{E_i}\right)^{1/2}.$$

$$\cdot \cos\Theta \exp\left\{-\left(\frac{E_i}{U}\right)^{3/2}\left[1 - \left(\frac{\Delta E_i}{E_i}\right)^{5/2}\right]\frac{1}{\cos\Theta}\right\}\sin\Theta d\Theta, \qquad (B12)$$

where

$$\Delta E_i = \frac{q^{3/2} F^{1/2}}{(\pi\varepsilon_r\varepsilon_0)^{1/2}},$$

$$U = \left(\frac{3q\hbar F}{4\sqrt{2m^*}}\right)^{2/3}, \qquad (B13)$$

$$m^* = \frac{m_e^* m_{lh}^*}{m_e^* + m_{lh}^*},$$

$E_i = E_g - E_T$ for electrons, $E_i = E_T$ for holes, and the last equation express the effective mass by electron effective mass and light hole mass.

The electron localized in the trap level can be also excited to the conduction band by tunnelling through the hyperbolic barrier with the contribution of phonons. To obtain a 3D tunnelling expression for electron emission rate with the

contribution of phonons, we adopt the results published by Rosencher *et al.* [37]

$$(e_n)_{PAT} = \frac{e_n^0}{2\pi} \exp\left(-\frac{E_g - E_T}{k_B T}\right) \int\limits_{\Delta E_i}^{E_i} \int\limits_{0}^{2\pi} d\phi \int\limits_{0}^{\pi/2} \cos\Theta \cdot$$

$$\cdot \exp\left\{\frac{F}{kT} - \left(\frac{E_g - E_T}{U}\right)^{3/2} \left[1 - \left(\frac{\Delta E_i}{E_g - E_T}\right)^{5/2}\right] \frac{1}{\cos\Theta}\right\} \cdot$$

$$\cdot \sin\Theta d\Theta \frac{dF}{kT}.$$

(B14)

For hole emission

$$(e_p)_{PAT} = \frac{e_p^0}{2\pi} \exp\left(-\frac{E_T}{k_B T}\right) \int\limits_{\Delta E_i}^{E_i} \int\limits_{0}^{2\pi} d\phi \int\limits_{0}^{\pi/2} \cos\Theta \cdot$$

$$\cdot \exp\left\{\frac{E}{kT} - \left(\frac{E_T}{U}\right)^{3/2} \left[1 - \left(\frac{\Delta E_i}{E_T}\right)^{5/2}\right] \frac{1}{\cos\Theta}\right\} \cdot$$

$$\cdot \sin\Theta d\Theta \frac{dE}{kT}.$$

(B15)

The total emission coefficient containing emission rates for the Pool-Frenkel effect, trap-assisted tunnelling, and phonon-assisted tunnelling is given by

$$(e_n)_{TOT} = (e_n)_{P-F} + (e_n)_{TAT} + (e_n)_{PAT}.$$

(B16)

The same relation is for holes.

Appendix C

Tunnelling generation for a triangular barrier

To calculate the tunnelling generation for the triangular barrier we follow a procedure described by Moll [26]. According to Moll's consideration, the incident electron flux per unit volume in a ring with perpendicular momentum $k_\perp$ to $k_\perp + dk_\perp$ is

$$\frac{q^2 F m^*}{2\pi^2 \hbar^3} f(\varepsilon) dE_\perp,$$

(C1)

where $f(\varepsilon)$ is the Fermi function.

The net tunnelling current density is equal to

$$\frac{dI}{A} = \frac{q^2 F m^*}{2\pi^2 \hbar^3} T_t \left[f(\varepsilon) - f'(\varepsilon)\right] dE_\perp dx,$$

(C2)

where $f(\varepsilon)$ and $f'(\varepsilon)$ are the Fermi functions on both sides of tunnelling (on the side from and into which tunnelling occurs).

For the triangular barrier (see Fig. C1), the tunnelling probability is

$$T_t = \exp\left[-2 \int\limits_{-x_1}^{x_2} \sqrt{\frac{2m^*}{\hbar^2}\left(\frac{E_g}{2} - qFx + E_\perp\right)}\right] =$$

$$= \exp\left[\frac{4\sqrt{2m^*}}{3qF\hbar}\left(\frac{E_g}{2} - qFx + E_\perp\right)^{3/2}\right]\Bigg|_{-x_1}^{x_2}.$$

(C3)

Taking into account the boundary conditions:

$$\frac{E_g}{2} - qFx + E_\perp = E_g + E_\perp, \quad \text{for} \quad x = -x_1, \quad \text{(C4)}$$

$$\frac{E_g}{2} - qFx + E_\perp \quad \text{for} \quad x = x_2 \quad \text{(C5)}$$

the tunnelling probablity is equal to

$$T_t = \exp\left(-\frac{4\sqrt{2m^*}}{3q\hbar F}\left(E_g + E_\perp\right)^{3/2}\right).$$

(C6)

Fig. C1. Triangular barrier

Equation (C2) can be expressed in an alternative form. Let ε be the energy at the edge of the forbidden. Then $qF = d\varepsilon/dx$ and

$$\frac{dI}{A} = \frac{qm^*}{2\pi^2 \hbar^3} \exp\left(-\frac{4\sqrt{2m^*}}{3q\hbar F}\left(E_g + E_\perp\right)^{3/2}\right) \cdot$$
$$\cdot \left[f(\varepsilon) - f'(\varepsilon)\right] dE_\perp d\varepsilon.$$

(C7)

The current density can be evaluated by a two-step integration. The first integration is carried out with respect to $E_\perp$ between the limits of 0 and $E_V - \varepsilon$, since larger values of $E_\perp$ place the electron in a forbidden state. The second integration with respect to energy is over the range $E_V < \varepsilon < E_C$. As was made by Moll [26], if the applied voltage is large compared to kT/q, the integration with respect to energy extends only from one Fermi level to the other in the classical turning points $- x_1$ and x_2. This difference in Fermi energy is marked as $\Delta\Phi$. In this approximation the current density

$$\frac{I(\varepsilon)}{A} = \frac{qm^*\bar{\varepsilon}}{3\pi^2 \hbar^3} \exp\left(-\frac{E_g}{\bar{\varepsilon}}\right) \Delta\Phi,$$

(C8)

where

$$\bar{\varepsilon} = \frac{3q\hbar F}{4\sqrt{2m^*}E_g^{1/2}}.$$

(C9)

The last term in Eq. (C8) arises from the finite limit that is placed on $E_\perp$ and in this case is negligible if $E_\perp \ll \Delta\Phi$. Finally, we have

$$\frac{I}{A} = \frac{q^2 (m^*)^{1/2} F \Delta\Phi}{4\sqrt{2}\pi^2 \hbar^2 E_g^{1/2}} \exp\left(-\frac{4\sqrt{2m^*}}{3q\hbar F}E_g^{3/2}\right),$$

(C10)

and using the STI procedure described by Adar [25], the tunnelling generation for the triangular barrier is equal to

$$G_{T_y}(F) = \frac{q^2 (m^*)^{1/2} F_y^2}{4\sqrt{2}\pi^2 \hbar^2 E_g^{1/2}} \exp - \left\{ \frac{4\sqrt{2m^*} E_g^{3/2}}{3qF_y\hbar} \right\}. \quad (C11)$$

REFERENCES

[1] M.A. Kinch, F. Aqariden, D. Chandra, P.-K. Liao, H.F. Schaake, and H.D. Shih, "Minority carrier lifetime in p-HgCdTe", *J. Electron. Mater.* 34, 880–884 (2005).

[2] O. Gravrand, L. Mollard, C. Largeron, N. Baier, E. Deborniol, and Ph. Chorier, "Study of LWIR and VLWIR focal plane array developments: comparison between p-on-n and different n-on-p technologies on LPE HgCdTe", *J. Electron. Mater.* 38, 1733–1740 (2009).

[3] G. Destefanis and J.P. Chamonal, "Large improvement in HgCdTe photovoltaic detector performances at LETI", *J. Electron. Mater.* 22, 1027–1032 (1993).

[4] W. Van Roosbroeck, "Theory of the electrons and holes in germanium and other semiconductors", *Bell Syst. Tech. J.* 29, 560–607 (1950).

[5] M. Kurata, *Numerical Analysis of Semiconductor Devices*, Lexington Books, Heath, 1982.

[6] H.K. Gummel, "A self-consistent iterative scheme for one-dimensional steady state transistor calculations", *IEEE Trans. Electron Devices* ED 11, 455–465 (1964).

[7] A. De Mari, "An accurate numerical steady-state one-dimensional solution of the p-n junction", *Solid State Electronics* 11, 33–58 (1968).

[8] Software: *Semicond Devices*, Dawn Technologies, Inc. California.

[9] Software: Apsys, *Crosslight Software*, Inc. Ontario, Canada.

[10] K. Jóźwikowski, J. Piotrowski, K. Adamiec, and A. Rogalski, "Computer simulation of HgCdTe photovoltaic devices based on complex heterostructures", *Proc. SPIE* 3629, 74–80 (1999).

[11] K. Jóźwikowski, "Computer simulation of non-cooled long wavelength multi-junction (Cd,Hg)Te photodiodes", *Infrared Phys.&Technol.* 41, 353–359 (2000).

[12] K. Jóźwikowski and A. Rogalski, "Effect of dislocations on performance of LWIR HgCdTe photodiodes", *J. Electron. Mater.* 29, 736–741 (2000).

[13] K. Jóźwikowski and A. Rogalski, "Computer modeling of dual-band HgCdTe photovoltaic detectors", *J. Appl. Phys.* 90, 1286–1291 (2001).

[14] K. Jóźwikowski, W. Gawron, J. Piotrowski, and A. Jóźwikowska, "Enhanced numerical modelling of non-cooled long-wavelength multi-junction (Cd,Hg)Te photodiodes", *IEEE Proc.-Circuits Devices Syst.* 150, 65–71 (2003).

[15] A. Jóźwikowska, K. Jóźwikowski, J. Rutkowski, Z. Orman, and A. Rogalski, "Generation-recombination effects in high temperature HgCdTe heterostructure photodiodes", *Opto-Electron. Rev.* 12, 417–428 (2004).

[16] A. Jóźwikowska, K. Jóźwikowski, J. Antoszewski, C.A. Musca, T. Nguyen, R.H. Sewell, J.M. Dell, L. Faraone, and Z. Orman, "Generation-recombination effects on dark current in CdTe passivated mid-wave infrared HgCdTe photodiodes", *J. Appl. Phys.* 98, 014504 (2005).

[17] K. Jóźwikowski, J. Piotrowski, W. Gawron, A. Rogalski, A. Piotrowski, J. Pawluczyk, A. Jóźwikowska, J. Rutkowski, and M. Kopytko, "Generation-recombination effect in high temperature HgCdTe heterostructure non-equilibrium photodiodes", *J. Electron. Mater.* 38, 1666–1676 (2009).

[18] J.S. Blakemore, *Semiconductor Statistic*, Pergamon Press, Oxford, 1962.

[19] R.J. McIntyre, "A new look at impact ionisation – Part I: A theory of gain, noise, breakdown probability and frequency response", *IEEE Trans. Electron Devices* 46, 1623–1631 (1999).

[20] M.A. Kinch, *Fundamentals of Infrared Detector Materials*, SPIE Press, Bellingham, 2007.

[21] A. Rogalski, K. Adamiec, and J. Rutkowski, *Narrow-Gap Semiconductor Photodiodes*, SPIE Press, Bellingham, 2000.

[22] E.O. Kane, "Tunneling in InSb", *J. Phys. Chem. Solids* 2, 181 (1960).

[23] E.O. Kane, "Theory of tunneling", *J. Appl. Phys.* 32, 83–91 (1961).

[24] C.B. Duke, *Tunneling in Solids*, Academic Press, New York, 1969.

[25] R. Adar, "Spatial integration of direct band-to-band tunnelling currents in general device structures", *IEEE Trans. Electron Devices* 39, 976–981 (1992).

[26] J.L. Moll, *Physics of Semiconductors*, McGraw-Hill, New York, 1964.

[27] C.H. Grein, M.E. Flatter, and Y. Chang, "Modeling of recombination in HgCdTe", *J. Electron. Mater.* 37, 1415–1419 (2008).

[28] A.S. Gilmore, J. Bangs, A. Gerrish, A. Stevens, and B. Starr, "Advancements in HgCdTe VLWIR materials", *Proc. SPIE* 5783, 223–230 (2005).

[29] T. Chuh, "Recent developments in infrared and visible imaging for astronomy, defense and homeland security", *Proc. SPIE* 5563, 19–34 (2004).

[30] J.A. Stobie, S.P. Tobin, P. Norton, M. Hutchins, K.-K. Wong, R.J. Huppi, and R. Huppi, "Update on the imaging sensor for GIFTS", *Proc. SPIE* 5543, 293–303 (2004).

[31] C.L. Jones, L.G. Hipwood, C.J. Shaw, J.P. Price, R.A. Catchpole, M. Ordish, C.D. Maxey, H.W. Lau, R.C. Mistry, M.C. Wilson, A.D. Parsons, J. Gillespie, L. Baggaley, and M. Wallis, "High performance MW and LW IRFPAs made from HgCdTe grown by MOVPE", *Proc. SPIE* 6206, 620610 (2006).

[32] W.E. Tennant, D. Lee, M. Zandian, E. Piquette, and M. Carmody, "MBE HgCdTe technology: a very general solution to IR detection, described by "Rule 07", a very convenient heuristic", *J. Electron. Mater.* 37, 1407–1410 (2008).

[33] W. Shockley and W.T. Read, "Statistics of recombinations of holes and electrons", *Phys. Rev.* 87, 835 (1952).

[34] Y. Nemirovsky, R. Fastow, M. Meyassed, and A. Unikovsky, "Trapping effect in HgCdTe", *J. Vac. Sci. Technol.* B9, 1829 (1991).

[35] S.E. Schacham and E. Finkman, "Recombination mechanisns in *p*-type HgCdTe: Freezout and background flux effects", *J. Appl. Phys.* 57, 2001–2009 (1985).

[36] J.L. Harthe, "The three-dimensional Poole-Frenkel effect", *J. Appl. Phys.* 39, 4871–4873 (1968).

[37] E. Rosencher, V. Mosser, and G. Vincent, "Transient-current study of field-assisted emission from shallow levels in silicon", *Phys. Rev.* B 29, 1135–1147 (1984).